Quantifying Surface Shelf Water Export in the southern Middle Atlantic Bight Using a Lagrangian Particle Tracking Approach

Shun Mao, Taylor Shropshire, and Ruoying He *

Department of Marine, Earth, and Atmospheric Sciences

North Carolina State University, Raleigh, NC 27695

*Corresponding author: Ruoying He (rhe@ncsu.edu)

Key Points:

- Three Middle Atlantic Bight shelf water export patterns linked to specific wind conditions are identified
- Lagrangian flow patterns of the MAB Shelf Water were notably impacted by 2017 and 2018 Atlantic Hurricane Seasons
- Sea Surface Velocity maps and Progressive Vector Diagrams reveal varied estuarine water pathways from Chesapeake and Delaware Bays.

Abstract

Shelf water is influenced by atmospheric forcing, river outflows, and the open ocean. Studying its variability is crucial for understanding anthropogenic impacts on coastal oceans and their transport to the open ocean. In the Middle Atlantic Bight (MAB), the interaction of the Gulf Stream with shelf/slope circulation leads to some of the complex exchanges between the shelf and open ocean along the U.S. East Coast. This study employs a Lagrangian particle tracking approach, grounded in a high-resolution, data-assimilative ocean reanalysis, to examine the export pathways of surface shelf water in the MAB. We analyzed over 700 daily images of simulated particle distributions using image clustering techniques. This revealed three distinct export patterns: abrupt entrainment to the Gulf Stream, gradual entrainment, and southern transport. Each pattern was observed roughly equally during the study period from January 2017 to December 2018. The observed export patterns are closely linked to the coastal circulation dynamics near Cape Hatteras. Understanding the timing and duration of these patterns is vital for assessing water quality and predicting the settlement of species that spawn in the region. Our study further underscores the influence of tropical cyclones, including Hurricanes Jose, Maria, and Chris, on these export patterns. These extreme weather events lead to significant shifts in coastal circulation near Cape Hatteras.

Plain Language Summary

This study focuses on the movement of ocean water in the Middle Atlantic Bight (MAB), a region along the U.S. east coast. The movement of this coastal water, or "shelf water," is affected by the weather, rivers, and the ocean. A Lagrangian particle tracking method was used to track the movement of water by simulating how particles move in the coastal ocean. Over 700 daily images of particle tracking simulations were obtained. Shelf water moves out of the MAB by three main pathways: abrupt entrainment, gradual entrainment, and southern transport. Each of these pathways happened about equally over two years (2017-2018). Understanding these water movements is key for knowing how long water stays in an area, which is important for water quality and for the life cycle of marine species that breed there. The study also highlights how tropical cyclones (like Hurricanes Jose, Maria, and Chris) can dramatically change these water movement patterns, especially near Cape Hatteras.

1. Introduction

The Middle Atlantic Bight (MAB) is a region of the U.S. East Coast that spans from North Carolina to Massachusetts. Most notably, this region creates a hotspot around Cape Hatteras for studying open ocean and coastal ocean interactions. These interactions create strong gradients and complex circulation, which when studied, help us to better understand underlying principles about the physics of open ocean and shelf water exchanges at broader scales. Globally these exchanges influence settlement of marine fauna (Epifanio, 1995; Shanks & Brink, 2005), fate of pollutants (Balthis, 2009; Moulton et al., 2023), and transfer of energy to the coastline (Brink, 2016). In the region surrounding Cape Hatteras, a significant amount of shelf water is often entrained and transported north due to the close approach of the Gulf Stream (GS) (Ford et al., 1952; Fisher, 1972). Hence studying MAB shelf water properties and dynamics is important locally, for downstream marine environments, and for more broadly understanding the oceanography of shelf exchange.

Cross-shelf exchange in the MAB has received considerable attention over the last three decades. Specifically, exchange has been shown to be influenced by GS variability (Churchill & Berger, 1998; Savidge & Bane, 2001; Churchill & Gawarkiewicz, 2012; Mao et al., 2023a), atmospheric forcing (Dirks et al., 1988; Glenn et al., 2016; Bane et al., 2023), and shelf water properties (Savidge et al., 2013; Savidge & Savidge, 2014). Significant advancements in understanding MAB shelf exchange have been achieved by four major observational programs:

- Mooring Observations (1992-1994): Funded by the Mineral Management Service (MMS), these observations focused on mass analyses of MAB water, highlighting its cold and fresh attributes (Berger et al., 1995).
- Ocean Margins Program (OMP) 1996: This program included two deployments of 26 moorings each, spanning from Cape Hatteras to Chesapeake Bay (Verity et al., 2002). Salinity band analysis of the OMP dataset by Churchill and Gawarkiewicz (2012) proposed an MAB shelf water export scheme. Most of the MAB shelf water entered the inner and middle Hatteras shelf, underwent entrainment by the GS, and was transported offshore to the northeast.
- Frontal Interaction Near Cape Hatteras (FINCH) Project: Conducted by collecting shipboard ADCP and towed CTD transect observations (Gawarkiewicz et al., 2008; Savidge & Austin, 2007), this project identified a shoreward transport of 0.05 Sv of Hatteras Front water in August 2004, driven by a dynamic height gradient due to varying water properties between MAB and South Atlantic Bight (SAB) shelf waters (Savidge & Austin, 2007).
- Processes Driving Exchange At Cape Hatteras (PEACH) Program (2016-2022): This comprehensive program investigated mechanisms and processes influencing shelf to open ocean exchanges near Cape Hatteras (Seim et al, 2022). Various observational platforms were utilized, including shipboard measurements (Andres et al., 2018; Mao et al., 2023b), bottom-mounted acoustic Doppler current profilers (Han et al., 2022), shore-based high-frequency radar observations (Haines et al., 2017), bottom-moored current and pressure sensor-equipped inverted echo sounders (CPIESs) (Andres et al., 2021), and glider missions (Todd, 2020a, b).

Despite these efforts, the actual spatial patterns that lead to MAB shelf water export have not been well documented. To date, drifter observations have provided some indications of export patterns. For example, Gawarkiewicz and Linder (2006) employed 42 satellite-tracked drifters to examine Lagrangian flow patterns in the southern MAB, identifying two major transport patterns. However, drifters are expensive to deploy, are quickly advected away from the region of interest, and typically are not feasible for continual deployment to identify local patterns over the course of seasons.

In this study, a Lagrangian particle tracking modeling framework is used to identify export patterns of MAB shelf water. Specifically, a high-resolution (800 m) data-assimilative ocean reanalysis is used along with the particle tracking framework OpenDrift (Dagestad et al., 2018) to simulate a two-year, continuous, near-surface particle evolution over the MAB and SAB continental shelf and slope from January 2017 through December 2018. Results from the particle tracking model are then used, along with image clustering techniques, to identify dominant spatial patterns of shelf water exchange. We also explores the mean transport pathways of estuarine water from the Chesapeake and Delaware Bay systems, which are significant estuarine systems on the East Coast serving as vital habitats for diverse marine species (Ruiz et al., 1993). By tracking particle displacement, we aim to illuminate the dynamics of water movement, including the dispersal of fish larvae and pollutants. Enhancing understanding of estuarine transport mechanisms help to support the broader implications for marine ecological management and conservation efforts (Cowen et al., 1993; Hare et al., 1996; Zhang et al., 2016).

2. Model and methods

2.1 Data-assimilative model

The ocean reanalysis used in this study was constructed by integrating a high-resolution regional ocean model (ROMS, Shchepetkin & McWilliams, 2005; Haidvogel et al., 2008) with an ensemble data assimilation approach that incorporates available remote and in-situ ocean observations from multiple platforms. The model assimilates sea level anomaly data from several satellites, including Jason-2, Jason-3, CryoSat-2, SARAL-AltiKa, Haiyang-2A, and Sentinel-3. It also assimilates daily sea surface temperature data sourced from the Advanced Very High Resolution Radiometer (AVHRR) managed by NOAA CoastWatch. In addition, observations from the PEACH project are incorporated, including high-frequency radar data, temperature and salinity profiles obtained through glider surveys and moorings, alongside buoy data from the National Data Buoy Center (NDBC) near Cape Hatteras. The model domain features a uniform horizontal resolution of 800 meters and 50 vertical layers, with enhanced resolution towards the surface and bottom boundary layers (**Figure 1a**). Atmospheric forcing data are obtained from the European Centre for Medium-Range Weather Forecasts (ECMWF) and ERA interim products, while global Hybrid Coordinate Ocean Model (HYCOM) data supplies model initial and boundary conditions. Thirteen major tidal constituents from the Finite Element Solution (FES) 2014 tide model (Lyard et al., 2021) are utilized for tidal forcing, and 22 estuary rivers from the National Water Model within the model domain are integrated for river forcing, by defining river runoff mass transport vertical profile and river runoff transport. The model's daily output spans from January 2017 to December 2018, aligning with the availability of in situ observations from the PEACH project.

2.2 Configuration of the OpenDrift framework

Particle tracking simulations are conducted using the Lagrangian software package OpenDrift (Dagestad et al., 2018). OpenDrift computes trajectories of drifting objects in the ocean using three-dimensional velocity fields, allowing for the tracking of water masses. Our particle tracking experiments are conducted at the surface ocean, focusing on diagnosing surface current dynamics. The sub-surface MAB shelf current dynamics is expected to be different due to its highly stratification characteristic in summer. To initially seed the model, approximately 4,200 neutrally buoyant surface particles are virtually released each day north of 36.8°N in MAB and SAB waters shallower than 100 m from January 1-10, 2017 (**Figure 2**). Because particles are quickly advected out of the target area, new particles are released into the surface ocean every three days throughout the two-year simulation. A batch size of 4,200 particles was selected because it sufficiently populated the region while maintaining computational efficiency. Our OpenDrift simulation ensures particles return to their prior position upon hitting the coast. This effectively simulates their movement away from the coast under offshore currents, avoiding onshore deposition. OpenDrift is run using a 6-hour time step with daily output. The decision to use a 6-hour time step was informed by the small impact of tidal currents in the Cape Hatteras region. The barotropic tidal velocities in the Cape Hatteras region are generally weak. Anders et al (2018) noted their contribution to velocities in this area is less than 0.1 cm/s, making the tidal effects negligible for the purposes of our study's focus on surface current dynamics over longer time scales and broader spatial extents. Once a particle exits the defined study area, its position is no longer tracked. We utilized as small a time step as possible and deployed a large number of particles, reaching into the millions, to enhance the statistical significance of the diagnosed pathways. However, we acknowledge that despite these efforts, our offline particle tracking simulation has limitations. Discussions in North et al.(2009), and Van Sebille et al.(2018), offers valuable insights into the challenges and limitations of particle tracking simulations. Dugstad et al. (2019) suggests that when dealing with model outputs that have both high resolution and high output frequency, as in our case, it's a customary practice not to apply additional diffusion.

2.3 Image clustering method

In the study area, over 700 daily snapshots of particle spatial distribution are generated. These daily images capture the horizontal distribution of MAB shelf water and are processed using image clustering to identify the dominant export patterns. Due to the complex circulation and lateral meanders of the GS near Cape Hatteras, conventional methods such as empirical orthogonal functions or self-organizing maps are not effective in extracting export patterns. In contrast, clustering techniques are well suited to identify complex patterns and are frequently used in machine learning and statistics (Kaufman & Rousseeuw, 2009).

In our application, clusters are composed of images showing similar Lagrangian flows. This offers insights into the prevailing export patterns and their temporal occurrence. Each daily image is dissected into a series of multidimensional vectors. These vectors encapsulate the distinct characteristics and flow patterns of the MAB shelf water for that day. During the clustering process, images are systematically compared against each other using similarity metrics to establish clusters that share flow patterns.

In our study, we used the same 800-m resolution for the clustering analysis. Each pixel is treated as a data point in a 2-dimensional space defined by latitude (p) and longitude (q). The pixel's intensity or color represents the distribution of particles. The intensity of each pixel is translated into a value between 0 (black, no particles) and 1 (white, maximum particle concentration). Consequently, each feature vector X_i within the image can be represented as:

$$X_i = (p_i, q_i, l_i) \tag{1}$$

where l_i is the intensity of the ith pixel. The k-means algorithm can then be applied to this set of feature vectors.

The first step is initialization. We randomly select k feature vectors from the dataset to serve as the initial centroids. Each centroid C_j, where j ranges from 1 to k, takes the form:

$$C_j = (c_{jp}, c_{jq}, c_{jl}) \quad (2)$$

The second step is assignment. This involves calculating the Euclidean distance between each data point and all the centroids, then assigning the data point to the centroid with the shortest distance.

$$D_{i,j,l} = sqrt((p_i - c_{jp})^2 + (q_i - c_{jq})^2 + (l_i - c_{jl})^2)) \quad (3)$$

Third, we update the new centroids by computing the mean of all data points in the cluster. The centroid of a cluster is the point that minimizes the total distance to all other points in the cluster, and it turns out that this point is simply the mean (average) of all points in the cluster.

$$c_{jp}\_new = mean(p_i) \quad (4)$$
$$c_{jq}\_new = mean(q_i) \quad (5)$$
$$c_{jl}\_new = mean(l_i) \quad (6)$$

Last, we repeat the assignment and update steps until the centroids do not change significantly. If the Euclidean distance between the positions of the centroids from one iteration to the next falls below 0.0001, we consider the centroids to have stabilized. Upon completion, the k-means algorithm will have divided the image into k clusters, each representing a region of the image with similar particle concentration. To conclude the clustering process, a cluster validation index is employed to determine the optimal quantity of clusters.

In our application, we utilize a pre-trained model known as VGG16 (Simonyan & Andrew, 2014) available in the Keras library. Keras is an open-source, deep learning library that provides a set of state-of-the-art deep learning models (Gulli et al., 2017; Ketkar et al., 2017). The image clustering process involves three steps: (1) importing a pre-trained VGG16 model; (2) employing the VGG16 model to extract features per image; and (3) applying k-means, a widely used unsupervised clustering method, to cluster the images (Dhanachandra et al., 2015).

Determining the optimal numbers of clusters was achieved using the Elbow Method (Nainggolan et al., 2019). We executed the k-means clustering algorithm for a range of k values. For every value of k, the sum of squared distances (SSE) is computed from each data point to its assigned centroid. By plotting the SSE values (Table 1) against the corresponding k values, the “elbow” point can be identified. Beyond this point, adding more clusters does not lead to a significant decrease in the SSE. For our particle distribution images, the optimal value of k was identified as 3.

3. Results

3.1 Model validation

A number of model-data comparisons were investigated to validate the model’s data assimilation and performance. To address data assimilation, the simulated sea surface temperature (SST) was compared to four buoys from the National Data Buoy Center (buoys 44014, 44095, 41064, and 41025; **Figure 1b**). Correlation coefficients were > 0.95 for all buoys except 41025, which had a coefficient of r = 0.73 (**Figure 3**). The lower correlation coefficient at buoy 41025 can be attributed to its proximity to the GS's separation point, where more dynamic and intricate interactions occur between the GS and adjacent shelf and slope waters near Cape Hatteras. Nevertheless, the high correlation coefficients indicate the ocean reanalysis effectively assimilates in-situ measurements.

Model performance was also evaluated using independent comparisons with unassimilated data as was done in He and Weisberg (2003). Simulated near-surface (at 5 m depth) currents were compared with in situ current measurements at two buoys north of Cape Hatteras (B1 and A4, see Figure 1b) and two to the south (A7 and B2. See Figure 1b). When averaged over the simulation period, both modeled and observed data consistently show a southward flow at B1 and A4, with complex correlation coefficients of 0.49 and 0.46, respectively (**Figures 4-5**). The model also performed reasonably well at capturing high frequency events in this region. For instance, in March 2018, a significant Nor'easter induced a large southward flow that was well represented by the model. Phase angles, which represent the directional difference between model predictions and observations, were +7.43° (B1) and +1.64° (A4), suggesting a slight eastward shift in the model-predicted current from the observed current.

In the southern region of the domain, there was a slight discrepancy between the observed and modeled mean flow (**Figures 6-7**). At sites A7 and B2, observations showed a weak mean northward flow, while the model showed a weak mean southward flow. However, complex correlation coefficients were 0.62 (A7) and 0.61 (B2), indicating a fairly strong positive correlation despite the small differences in mean flow. Phase angles were -2.57° (A7) and -1.21° (B2), suggesting a small directional shift between the model and observed data. Overall, the model solution demonstrates a reasonable level of agreement with in-situ measurements in terms of both magnitude and direction of near-surface velocity.

3.2 Export patterns

In our thorough examination of circulation patterns using cluster configurations k=2, k=3, and k=4, we observed that k=2 successfully captures southward transport and abrupt entrainment. However, it overlooks the gradual entrainment process that is essential for understanding the trajectory of MAB shelf water towards the outer MAB shelf and into the Slope Sea. As for the scenario with k=4 while it similarly identifies the southward transport and abrupt entrainment processes, it goes further by distinguishing two closely related patterns in coastal circulation. One pattern shows shelf flow ranging from 35.5°N to 36.5°N with an east-southeast direction (112.5° clockwise from the north), while the second pattern exhibits an southeast flow direction (135° clockwise from the north). Therefore, we conclude that k=3 is the optimal cluster number, providing a balanced and clear depiction of circulation patterns near Cape Hatteras.

Three export patterns for MAB shelf water were identified by the image clustering analysis (**Figures 8-10**). Over the two-year study period, the occurrence of each export pattern is remarkably similar: 31.62%, 33.15% and 35.64% for Patterns 1, 2, and 3, respectively (described below). The southward entrainment pattern is more straightforward than the other two, describing the transport of MAB shelf water southward into the SAB and its subsequent entrainment by the GS into the open ocean. Regarding the abrupt entrainment, the curvature radius near 35.5°N is approximately 0.5 degrees (~55 km), with surface particle entrainment speeds reaching 1-1.5 m/s. For the gradual entrainment, the curvature radius near 36.5°N is about 0.75 degrees (~85 km), and the surface particle entrainment speeds are approximately 0.2-0.4 m/s. Each pattern reveals an underlying forcing mechanism with clear temporal variability. This results in the persistence of a single pattern for specific periods followed by transition periods from one pattern to the next (**Figure 11**). To better interpret these mechanisms, composite mean circulation and wind anomaly fields (relative to mean wind condition for each pattern) were analyzed during each export pattern (**Figure 12**).

Pattern 1: "Abrupt entrainment." This pattern is characterized by the rapid entrainment of shelf water into the GS, predominantly taking place from April to September (**Figure 11**), when prevailing winds are southwesterly during spring and summer (**Figure 12a**). Throughout this period, the seasonal wind forcing significantly influences the circulation around Cape Hatteras. As a result, southward-moving MAB shelf water and northward-flowing SAB shelf water converge north of Cape Hatteras, near 35.5°N. This distinctive configuration of shelf circulation sets the stage for the abrupt entrainment of MAB shelf water into the GS (**Figure 8**).

Pattern 2: "Gradual entrainment." This pattern emerges primarily in the first half of the year (January - May) during the winter - spring transition (**Figure 11**). Throughout this period, the prevailing wind is westerly, causing the shelf surface water to move more consistently and gradually offshore relative to Pattern 1(**Figure 12b**). In this Pattern, a significant portion of MAB shelf water is directed towards the outer MAB shelf then enters the Slope Sea, where it eventually gets swept northeast by the GS (**Figure 9**). This circulation results in particle tracks exhibiting relatively large radii of curvature, a defining feature of Pattern 2.

Pattern 3: "Southward transport." This pattern is characterized by the southward extension of MAB shelf water into the SAB and is prominent during the late fall and winter (**Figure 11**). During this period, prevailing winds are primarily northeasterly, resulting in robust coastal downwelling and a southward flow around Cape Hatteras (**Figure 12c**). Driven by wind-induced transport, particle trajectories extend further southward, reaching as far as Long Bay, South Carolina, before being drawn into the GS (**Figure 10**). During this pattern, the GS's velocity is slower than in Patterns 1 and 2.

3.3 Mean estuarine water transport pathways

In this section, we examine the mean transport pathways of estuarine water from the Chesapeake and Delaware Bay systems. The analysis is based on the composite mean Sea Surface Velocity (SSV) fields (**Figure 12**). To achieve this, we employ Progressive Vector Diagrams (PVDs) in an idealized experimental setup. This approach contrasts with the realistic OpenDrift particle tracking experiment and is specifically designed to provide insight into movement of estuarine water, such as fish larvae and pollutants.

In our analysis, we specifically track the displacement of particles, depicted as blue filled circles in **Figure 13**, released from both Chesapeake and Delaware Bays over a 45-day interval. These particle displacements are driven by the three composite mean SSV patterns (highlighted in Figure 12). The composite mean SSV fields are derived by averaging velocities throughout each pattern period. PVDs are utilized to calculate and illustrate the historical trajectories of the released particles (Figure 13). Due to the large number of particles, only daily tracking results are shown.

The methodology of PVD can be outlined as follows: Considering the equation for displacement, x_n and y_n represent longitudinal and latitudinal particle locations, respectively. U_0 and V_0 denote the respective composite mean SSV field. Each n represents a specific time step, and Δt is the duration between steps. We used Δt = 1 day during the PVD calculation. The equations are:

$$x_n = x_{n-1} + U_0 * \Delta t \tag{7}$$

$$y_n = y_{n-1} + V_0 * \Delta t \tag{8}$$

Particle motion can be represented by displacement vectors:

$$Sn = (x_n, y_n) \tag{9}$$

Marine larvae often spend 30-60 days in the water column (Strathmann, 1985; Jablonski, 1986; Wellington & Robertson, 2001). Therefore, we chose 45 days as a typical PVD integration period. After 45 days, the PVDs corresponding to the abrupt entrainment pattern (Pattern 1; green dots in **Figures 13a, b**) and southward transport pattern (Pattern 3; green dots in **Figures 13e, f**) show similar movement of estuarine water originating from Chesapeake Bay and Delaware Bay. These estuarine waters are transported further south by MAB shelf flow before ultimately becoming entrained by the GS offshore of Cape Hatteras. This entrainment of estuarine water typically takes place between latitudes 35.5°N and 36°N. The diagrams also indicate that estuarine water from the MAB does not enter the SAB region when influenced by the average SSV pattern. However, when subjected to a strong atmospheric forcing event near Cape Hatteras, MAB estuarine water may enter the SAB region.

In contrast, the gradual entrainment pattern (Pattern 2) shows more direct offshore entrainment of MAB estuarine water transport. Driven by averaged SSV of gradual entrainment (Pattern 2), both the Chesapeake and Delaware estuarine waters (**Figures 13c, d**) are transported eastward over the MAB shelf initially. For the Chesapeake, its estuarine water is entrained by the GS within latitudes 36°N to 36.5°N, while the Delaware estuarine water is transported by the shelfbreak jet and slope sea gyre before being entrained by the GS near 37°N. This estuarine water entrainment is evident in the larger radii of curvature displayed by the drifter tracks.

The Coastal Pioneer Array (black dots in Figure 13) has been operational since spring 2024 to collect new oceanographic observations in the southern MAB. Our results suggest that this mooring array would effectively capture both Chesapeake and Delaware estuarine water exports near Cape Hatteras during abrupt entrainment (Pattern 1) and southward transport (Pattern 3) patterns. However, it might not capture the freshwater export during the gradual entrainment (Pattern 2). Mobile platforms such as gliders and autonomous underwater vehicles could provide valuable observations of the shelf-open ocean exchange between 36.5°N and 37.75°N.

4. Discussions

4.1 Export patterns in relation to an earlier study

Export patterns identified in this study align well with previous field observations. Using satellite-tracked drifters, Gawarkiewicz and Linder (2006) identified two major transport patterns (abrupt and gradual entrainment) and two rarer cases of MAB shelf water transport. The two major patterns in the aforementioned study are characterized by small and large radii of curvature, which closely resemble our Pattern 1 (abrupt entrainment) and Pattern 2 (gradual entrainment), respectively. Abrupt entrainment frequently occurred within the latitudinal range of 35.4°N to 36.5°N. A defining characteristic of this pattern is the small radii of curvature evident in drifter tracks within this region, indicating a swift and almost instantaneous merging of MAB shelf water with the GS as it approaches Cape Hatteras. In contrast, the gradual entrainment pattern is reflected in the larger radii of curvature observed in the drifter tracks and frequently occurred between 35.7°N and 37°N. Gawarkiewicz and Linder (2006) documented two rare cases where drifters traveled southward across Cape Hatteras, diverging from typical patterns observed in the region. These drifter tracks align with the pathway described in our southward transport pattern. Unlike the abrupt or gradual entrainment patterns, MAB shelf water that moves south of Cape Hatteras quickly becomes entrained by the GS.

4.2 Image clustering application in oceanography

Although seldom employed in oceanography, utilizing image-clustering methods to investigate circulation patterns presents several advantages. First, image clustering improves pattern recognition. Such algorithms excel at detecting patterns within complex datasets, allowing them to identify similar trajectories, group them together, and thus help delineate circulation patterns. Second, image clustering aids in quantifying transport mechanisms. These algorithms can identify the various dominant flows of shelf water that drive the export pattern of MAB shelf water. Lastly, image-clustering can enable time-evolution analysis, providing insights into the progression of Lagrangian transport patterns over time. To ensure more robust results, future studies should continue to leverage image-clustering methods for identifying dominant circulation patterns over extended time spans.

4.3 Estuarine water transport and potential ecological impacts

Estuaries are known to be important nursery grounds for a diverse range of fish species, each with varying levels of dependence on these habitats (Able, 2005; Whitfield, 2021). This is underscored by the behavior of some species that, while not residing in estuaries, migrate into them and nearby areas to spawn (Warlen & Burke, 1990). Furthermore, the early life stages of some species that spawn offshore are found in estuaries and subsequently migrate back offshore as they mature (Pattrick & Stydom, 2014). Consequently, understanding the transport of water to the mouth of estuaries and away from estuaries is vital for comprehending population connectivity. Results from this study elucidate mechanisms that influence the latter.

One salient discovery from the current study is that, under typical (mean) conditions, estuarine water from the MAB does not enter the SAB region within 45 days for any of the three export patterns. Many species have pelagic larval durations shorter than 45 days. Following the larval phase, they require a substrate for further development. This implies that species spawning in estuaries, whose habitat ranges span both north and south of Cape Hatteras, either:

(1) populate regions south of Cape Hatteras via southern movement of adults that initially developed from larvae settled north of Cape Hatteras;

(2) have spawning locations south of Cape Hatteras;

(3) rely on sub-surface currents to transport larvae from the MAB to the SAB; or

(4) depend heavily on sporadic, high-intensity ocean circulation caused by extreme weather conditions that transport larvae from the MAB to the SAB.

Future modeling endeavors could integrate vertical motion into Lagrangian simulations to refine these hypotheses.

Another significant finding is that, under Pattern 2, larvae consistently move offshore, eventually becoming entrained in the GS. Years dominated by this circulation pattern may profoundly influence the abundance of new fish entering a population (recruits). Such information can be harnessed to generate environmental indices useful in fisheries management. Further exploration is needed to examine the relationship and frequency of export patterns and the recruitment of species to the MAB and SAB.

4.4 Impacts of tropical cyclones

The 2017 and 2018 Atlantic hurricane seasons notably impacted the Lagrangian flow patterns of MAB shelf water, especially when four tropical cyclones entered our study domain near Cape Hatteras (**Figure 14**).

In September 2017, Hurricanes Jose and Maria followed a roughly northward track from 28°N to 36°N on the eastern flank of the GS. While Hurricane Jose decelerated and dissipated south of New England after crossing the GS, Hurricane Maria turned sharply eastward and gradually weakened. Their collective influence intensified northeasterly winds over the MAB shelf and coastal circulation near Cape Hatteras. In October 2017 (Figure 10d), an extreme southward movement of MAB shelf water was evident, extending to both Onslow Bay and Long Bay south of Cape Hatteras.

On July 6, 2018, a tropical depression formed south-southeast of Cape Hatteras, and later intensified into Tropical Storm Chris. Chris followed a northeastward trajectory over the Atlantic Ocean before eventually dissipating. When this low-pressure system passed approximately 500 kilometers south-southeast of Cape Hatteras, it altered the MAB shelf flow pattern (Figure 11) from the abrupt entrainment pattern (Pattern 1 in Figure 15a) to the southward transport pattern (Pattern 3 in Figure 15b). Once Chris dissipated, Pattern 1 resumed.

Hurricane Florence made landfall on September 14, 2018, and its effects were substantial. The storm lingered over the Carolinas due to synoptic-scale interactions (Zambon et al., 2021), leading to record-breaking rainfall. Prior to Florence's impact, MAB shelf waters were entrained into the GS south of Cape Hatteras (Pattern 3). However, Florence's slow movement onshore altered the dynamics, leading to MAB shelf waters being constrained to export north of Cape Hatteras (Pattern 1). The shift in the export configuration from Pattern-3 (Figure 15c) to the abrupt entrainment Pattern -1 (Figure 15d) was a result of Florence's influence. During this period, Florence also brought unprecedented rainfall to North and South Carolina from mid-September to early October. Export returned to Pattern 3 once Florence’s impacts subsided.

5. Summary

Through our application of Lagrangian particle tracking, grounded in a high-resolution, data-assimilative ocean reanalysis, in conjunction with image clustering analyses, we extracted three distinct patterns of MAB shelf water export during 2017-2018. Each of these patterns is associated with specific surface wind forcing: 1) Abrupt entrainment (Pattern 1) is associated with southwesterly wind from April to September. This pattern, covering 31.62% of the study period, is marked by shelf water particles undergoing rapid entrainment between 35.4°N and 36.5°N. 2)

Gradual entrainment (Pattern 2) is associated with westerly winds during January - May (winter - spring) seasonal transition. Constituting 33.15% of the instances, this pattern features particles gradually entraining between 35.7°N and 37°N. 3) Southward transport (Pattern 3) is associated with strong northeasterly wind during the late fall - winter season. It accounts for 35.64% of the instances, with the MAB shelf waters moving southward across Cape Hatteras before ultimately being entrained by the GS. Additionally, extreme weather events such as tropical cyclones exert significant influence in shifting the export patterns of MAB shelf water.

Composite Sea Surface Velocity (SSV) field maps, along with their corresponding Progressive Vector Diagrams (PVD), help shed light on the mean export pathways of estuarine water from Chesapeake and Delaware Bays. Under the influence of the composite mean SSV from both the abrupt entrainment (Pattern 1) and southward transport (Pattern 3), these estuarine waters flow south through MAB shelf, and are then drawn offshore by the GS near Cape Hatteras, within the 35.5°N to 36°N range. In contrast, during the gradual entrainment (Pattern 2), estuarine waters primarily move eastward across the MAB shelf. Waters from Chesapeake Bay merge with the GS between 36°N and 36.5°N, while waters from Delaware Bay are carried by the shelfbreak jet and slope sea gyre before being entrained by the GS offshore near 37°N.

The Coastal Pioneer Array commissioned in spring 2024, is currently monitoring exports of both Chesapeake and Delaware estuarine water near Cape Hatteras during the phases of abrupt entrainment (Pattern 1) and southward transport (Pattern 3). However, to gain a clearer understanding during gradual entrainment (Pattern 2), especially for observations of shelf-open ocean exchange between 36.5°N and 37.75°N, supplementary mobile platforms like gliders and autonomous underwater vehicles will be essential.

In summary, this study unveils new insights into the predominant pathways and export patterns that govern the dynamics of near-surface MAB shelf water. It also highlights an innovative application of deep-learning image clustering techniques to coastal circulation studies. Building upon our findings, future research can utilize our particle-tracking framework to examine the export pathways of subsurface water masses throughout the MAB shelf and to investigate the complex dynamics of shelf water subduction as it interacts with the slope sea and the GS. Additionally, these studies are poised to yield new insights into potential larval transport pathways and population connectivity, which are crucial for sustainable fisheries management. Regarding future research, besides examining the residence time of specific water masses over the continental shelf and Slope Sea, the analytical techniques described by van Sebille et al. (2018) also facilitate the study of age distributions, probability characteristics, and biological interactions of these water masses. These methodologies can be further applied to investigate the dynamics between the shelf and the open ocean at the southern boundary of the MAB.

Acknowledgements:

Research support provided through NSF grant OCE-1559178 and OCE-1851421, RISE-2019758, OCE-2206052, CNS-2223844, NOAA grant NA16NOS0120028 is much appreciated. We thank Drs. Glen Gawarkiewicz, John Wilkin, Al Plueddemann, John Bane, and Harvey Seim for many insightful discussions throughout this study. We thank Jennifer Warrillow for her editorial assistance.

Open Research and Data Availability Statement:

The two –year dataset of particle spatial distribution is available from Mao and He (2024a). The computer source codes used to create particle spatial distribution is available from Mao and He (2024b). The Regional Ocean Modeling System (ROMS) configuration setup is available from Mao and He (2024c). The corresponding ROMS output is available from Mao and He (2024d).

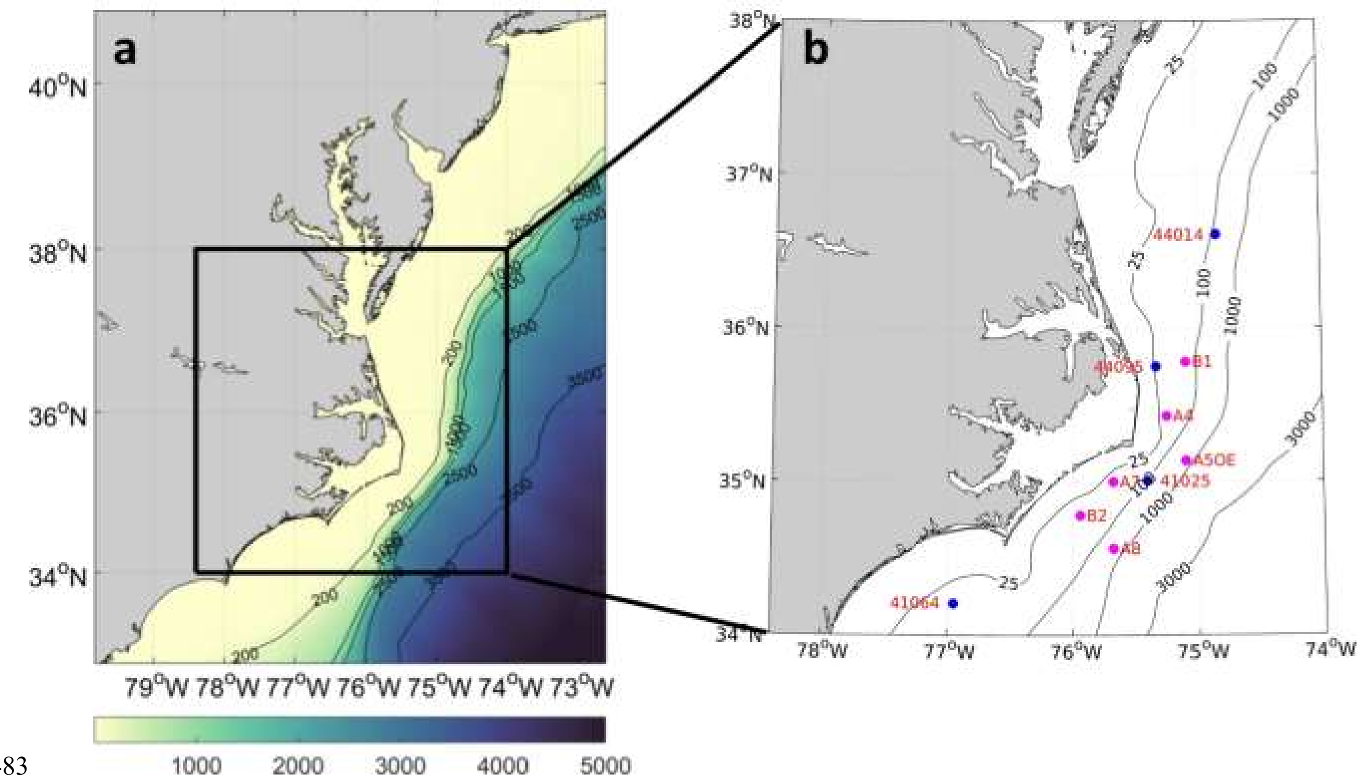

Figure 1. Panel (a): Modeling domain. Isobaths of 200 m, 1000 m, 1500 m, 2500 m, and 2500 m are denoted with black solid lines. Panel (b): Notable observational sites in this study from PEACH project: four buoys from National Data Buoy Center (NDBC) are denoted with blue circles; B1 and B2 are two meteorological buoys with in-water CTDs, denoted with red circles; A4, A5OE, A7 and A8 are mooring Acoustic Doppler Current Profilers (ADCPs), denoted with red circles.

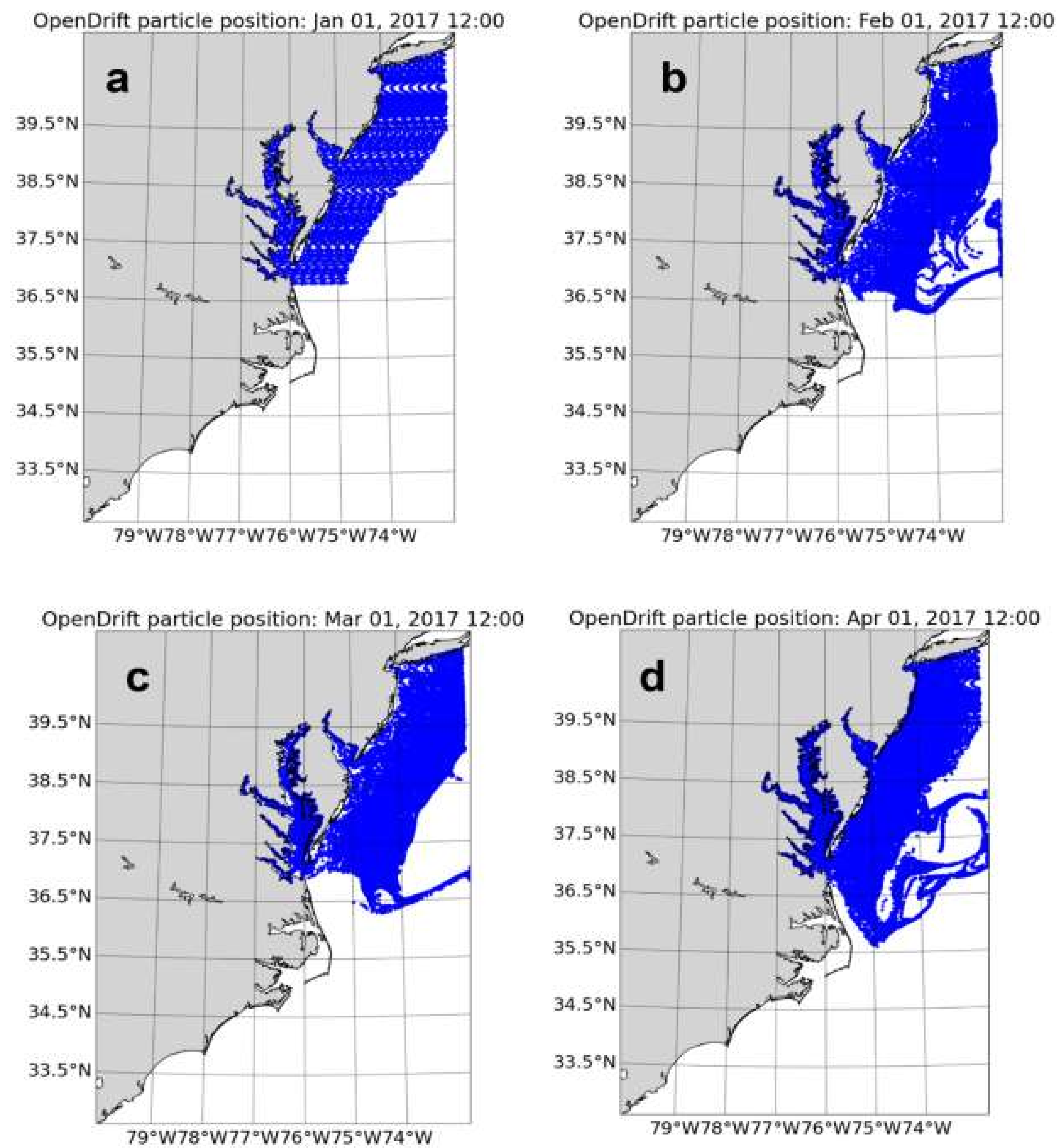

Figure 2. Panel (a): Initial particle locations on January 1, 2017. These particles are located within the 100 m isobath, north of 36.8ºN, in the model domain. The same number of particles are released every three days at the same locations during particle tracking simulations. Panels (b), (c), and (d) show the horizontal distribution of near-surface MAB shelf water on February 1, March 1, and April 1, 2017, respectively.

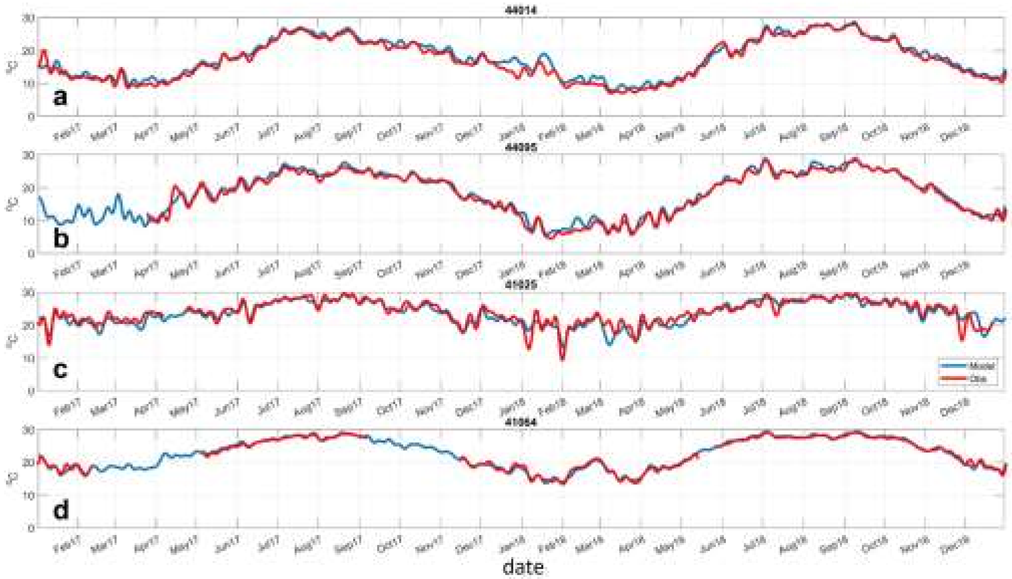

Figure 3. Sea surface temperature comparisons between model results (blue lines) and in situ observations (red lines). Panel (a), (b), (c) and (d) show comparison at NDBC buoys 44014, 44095, 41025 and 41064, respectively. A 7-day low-pass filter has been applied to both observations and modeling results.

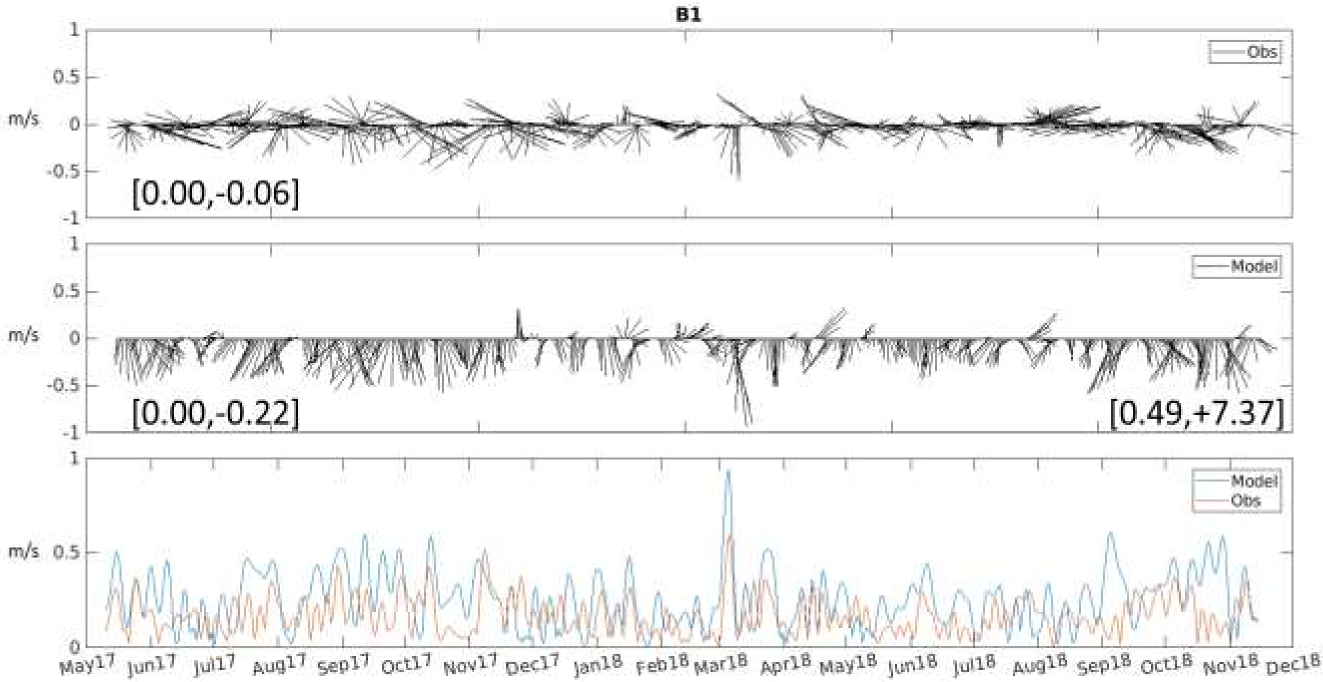

Figure 4. Comparisons of near-surface (at 5 m depth) current at buoy B1 from model results and in-situ observations, with a 7-day low-pass filter applied to both. The upper and middle panels display the velocity vectors of the observed and modeled current time series, respectively, from April 2017 to November 2018. The 19-month mean eastward and northward velocity components are presented in the bottom left corner of each panel. The comparison between the model and data is quantified using the squared complex correlation coefficient and phase angle. Both values are displayed in the bottom right corner of the middle panel. The lower panel shows a comparison of the mean current component (u, v) magnitudes derived from both the model results (blue line) and observations (red line).

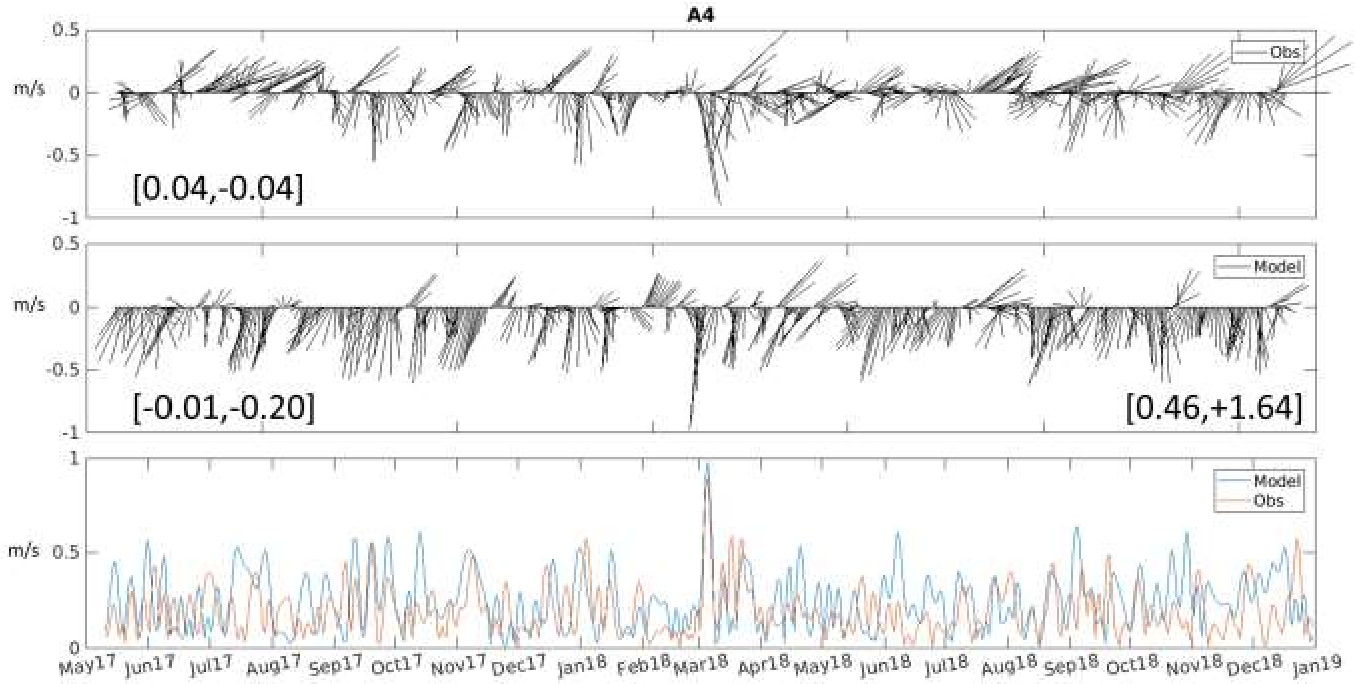

Figure 5. Same as Figure 4, but for site A4.

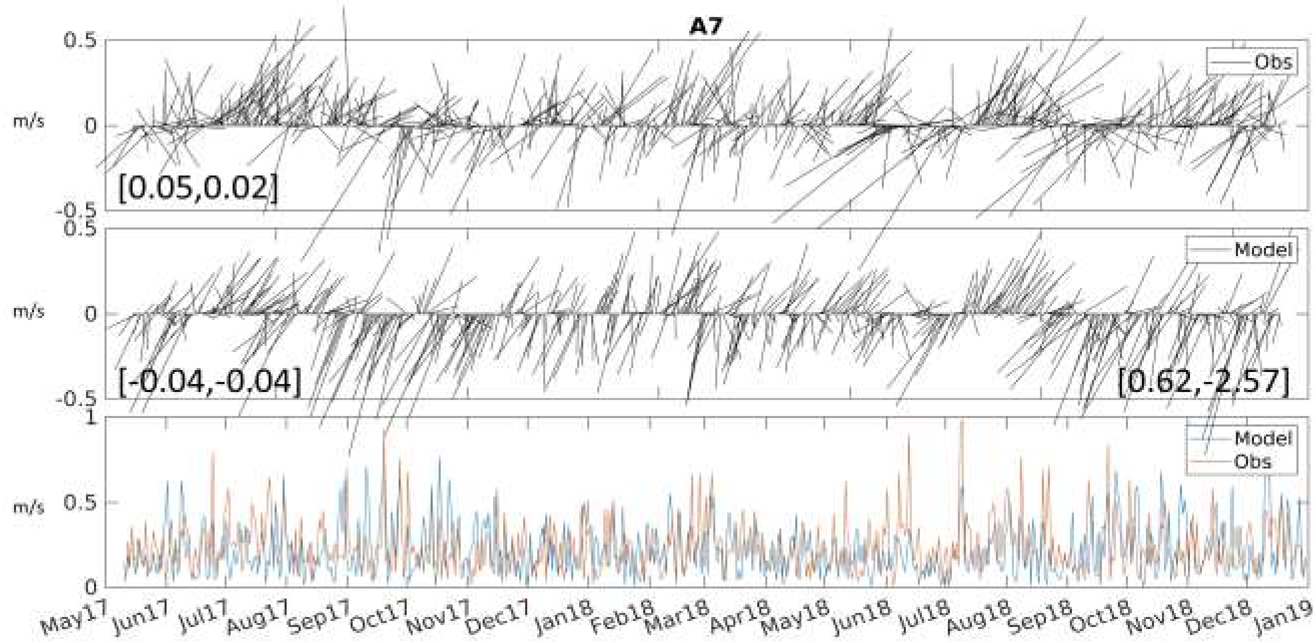

520 **Figure 6.** Same as Figure 4, but for site A7. For better visualization, both observed and modeled
521 vectors are rotated 45º counterclockwise (upper and middle panel).
522

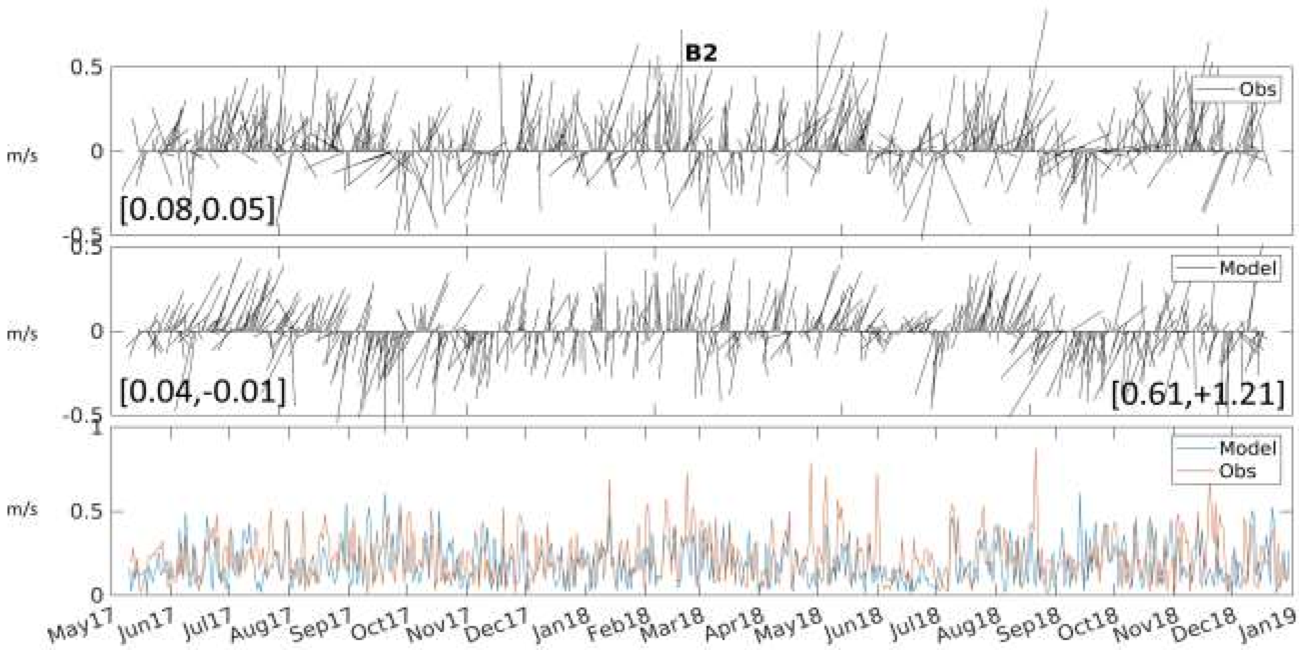

524 **Figure 7.** Same as Figure 4, but for site B2. For better visualization, both observed and modeled
525 vectors are rotated 45 º counterclockwise (upper and middle panel).

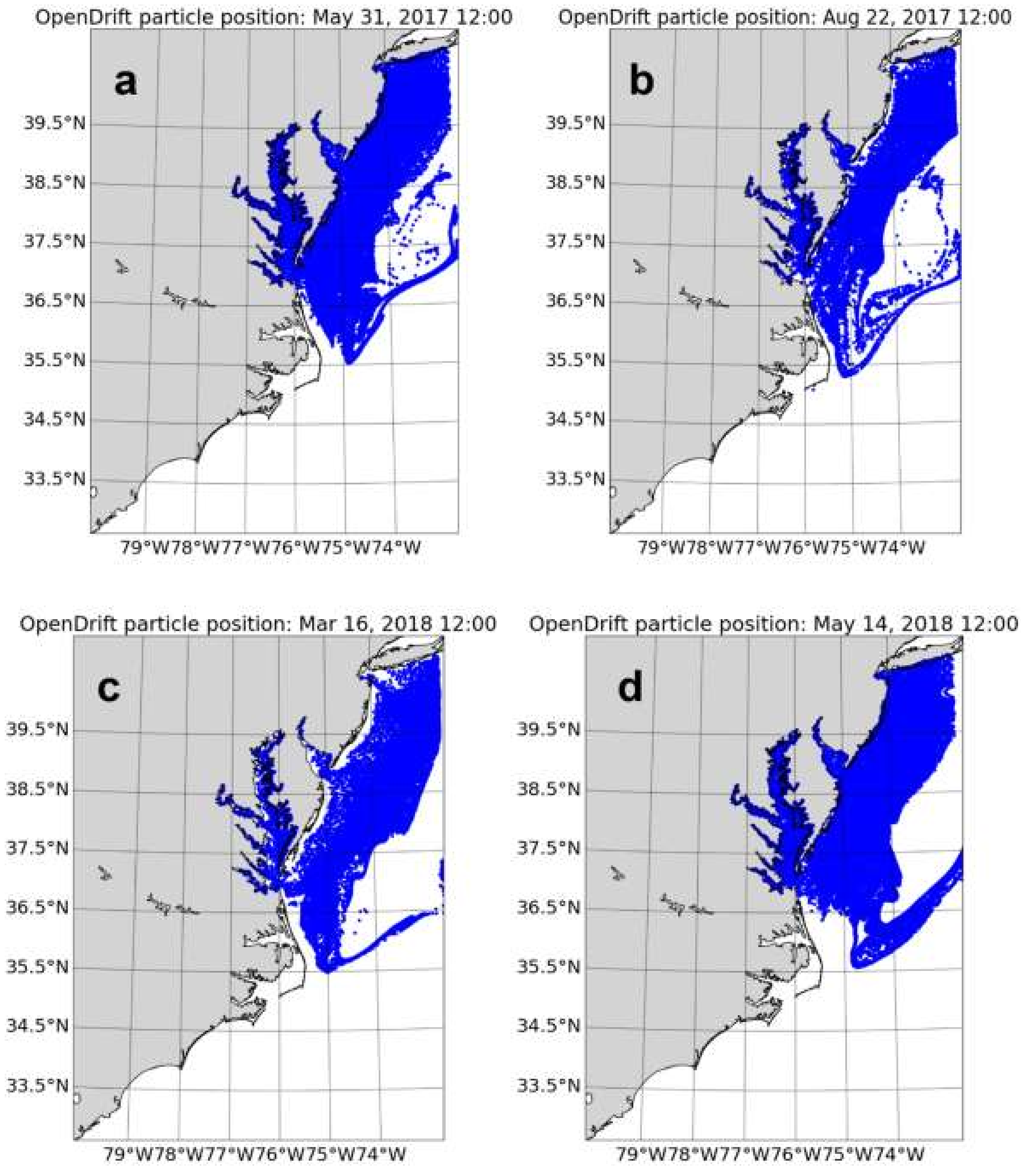

Figure 8. Pattern 1, "abrupt entrainment," of MAB shelf water Lagrangian flow. Panels show snapshots of horizontal distribution of near-surface MAB shelf water on May 31, 2017; August 22, 2017; March 16, 2018; and May 14, 2018, respectively.

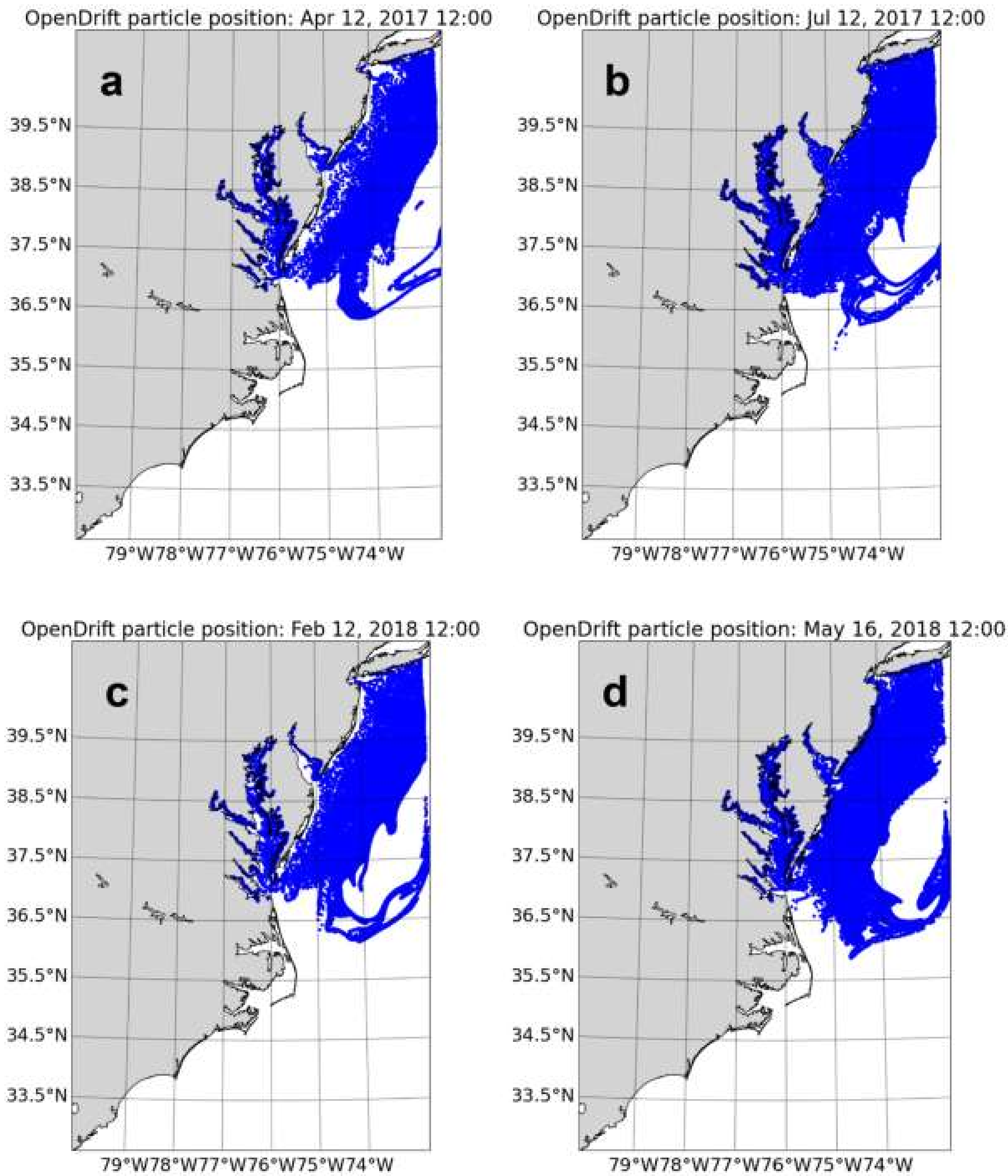

Figure 9. Pattern 2, "gradual entrainment," of MAB shelf water Lagrangian flow. Panels show snapshots of horizontal distribution of near-surface MAB shelf water on April 12, 2017; July 12, 2017; February 12, 2018; and May 16, 2018, respectively.

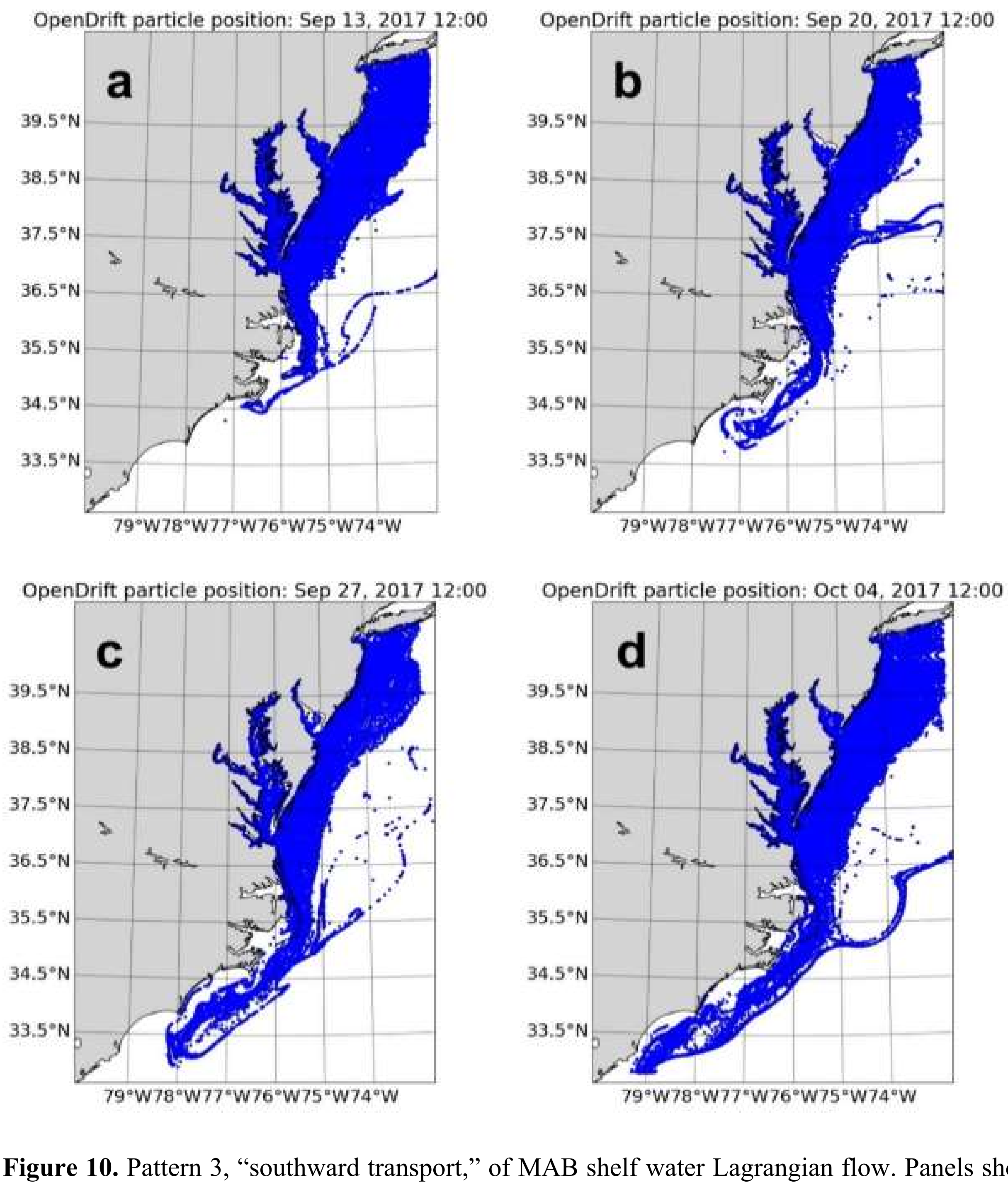

Figure 10. Pattern 3, "southward transport," of MAB shelf water Lagrangian flow. Panels show snapshots of horizontal distribution of near-surface MAB shelf water on September 13, 2017; September 20, 2017; September 27, 2017; and October 4, 2017, respectively.

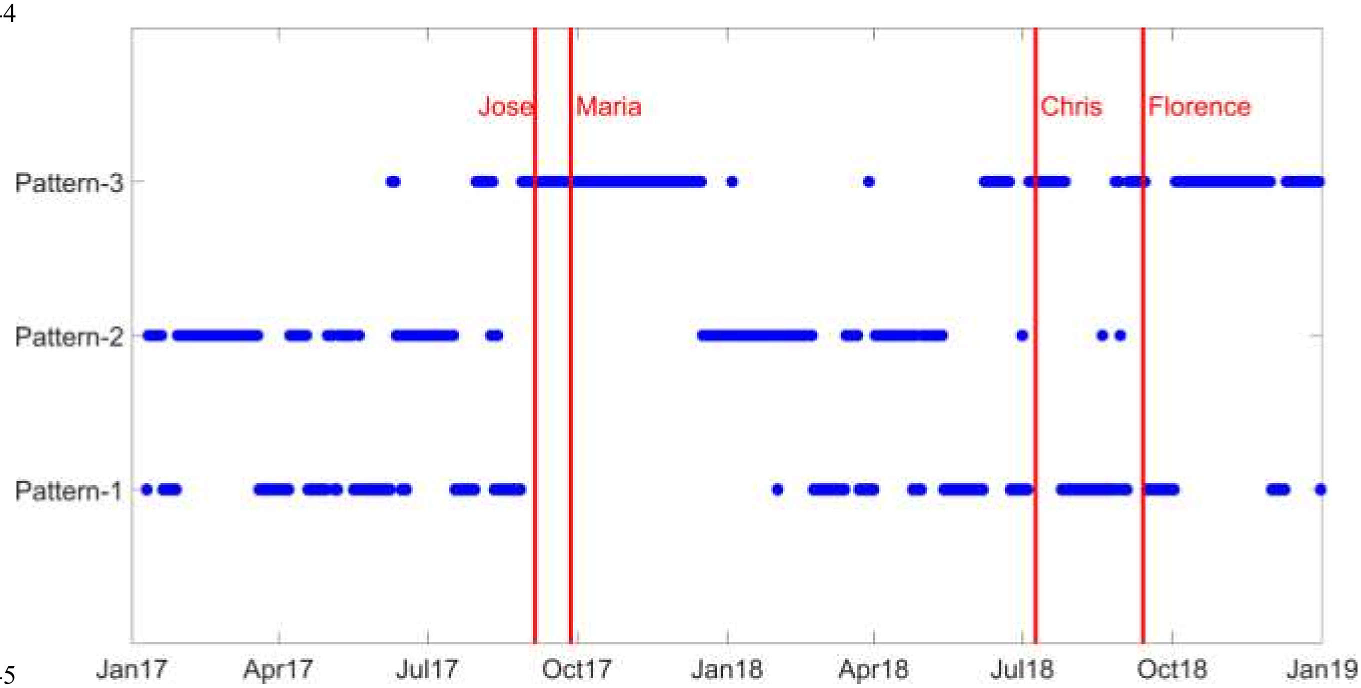

Figure 11. Time series of three MAB shelf water Lagrangian flow patterns from Jan. 2017 to Dec. 2018. Hurricane Jose, Maria, Chris, Florence, and Michael are indicated by vertical lines.

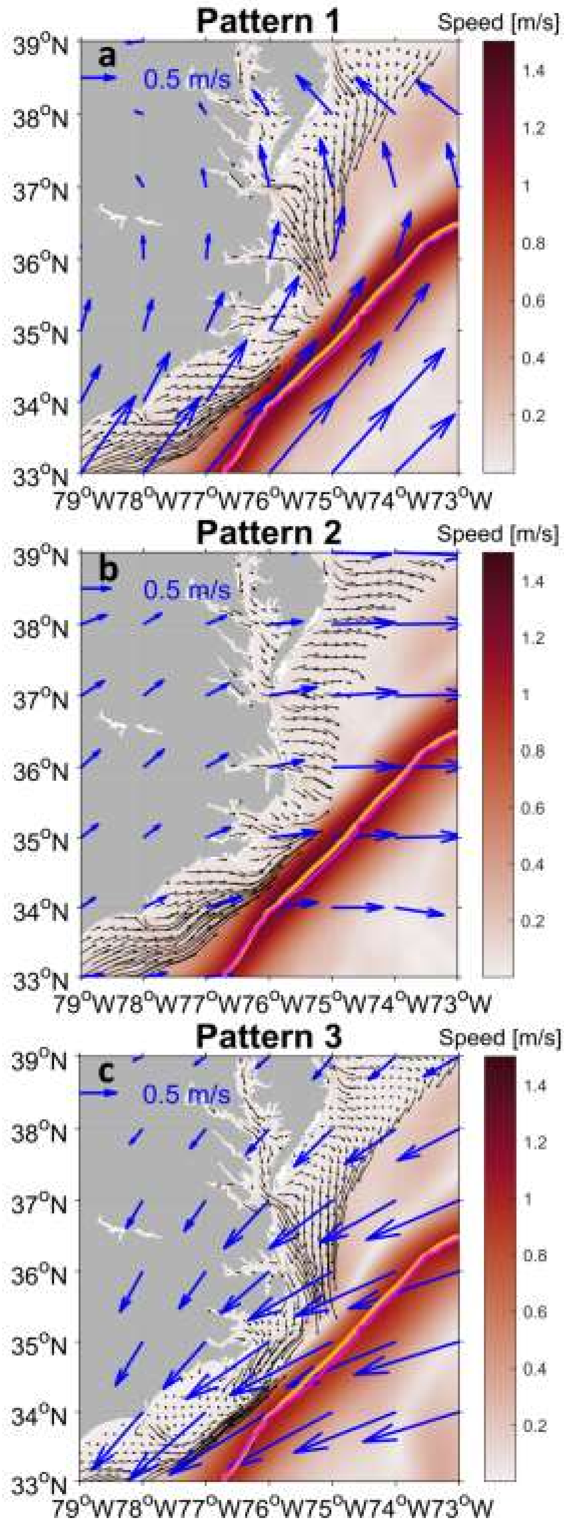

Figure 12. Composite mean maps of sea surface velocity (SSV) fields near Cape Hatteras based on three export patterns. The SSV fields for patterns 1, 2, and 3 are shown in (a), (b), and (c), respectively. Wind anomaly vectors during each pattern period are overlaid (blue vectors). Orange solid lines denote the two-year mean GS path during 2017-2018 and magenta solid lines denote mean GS path during each pattern period.

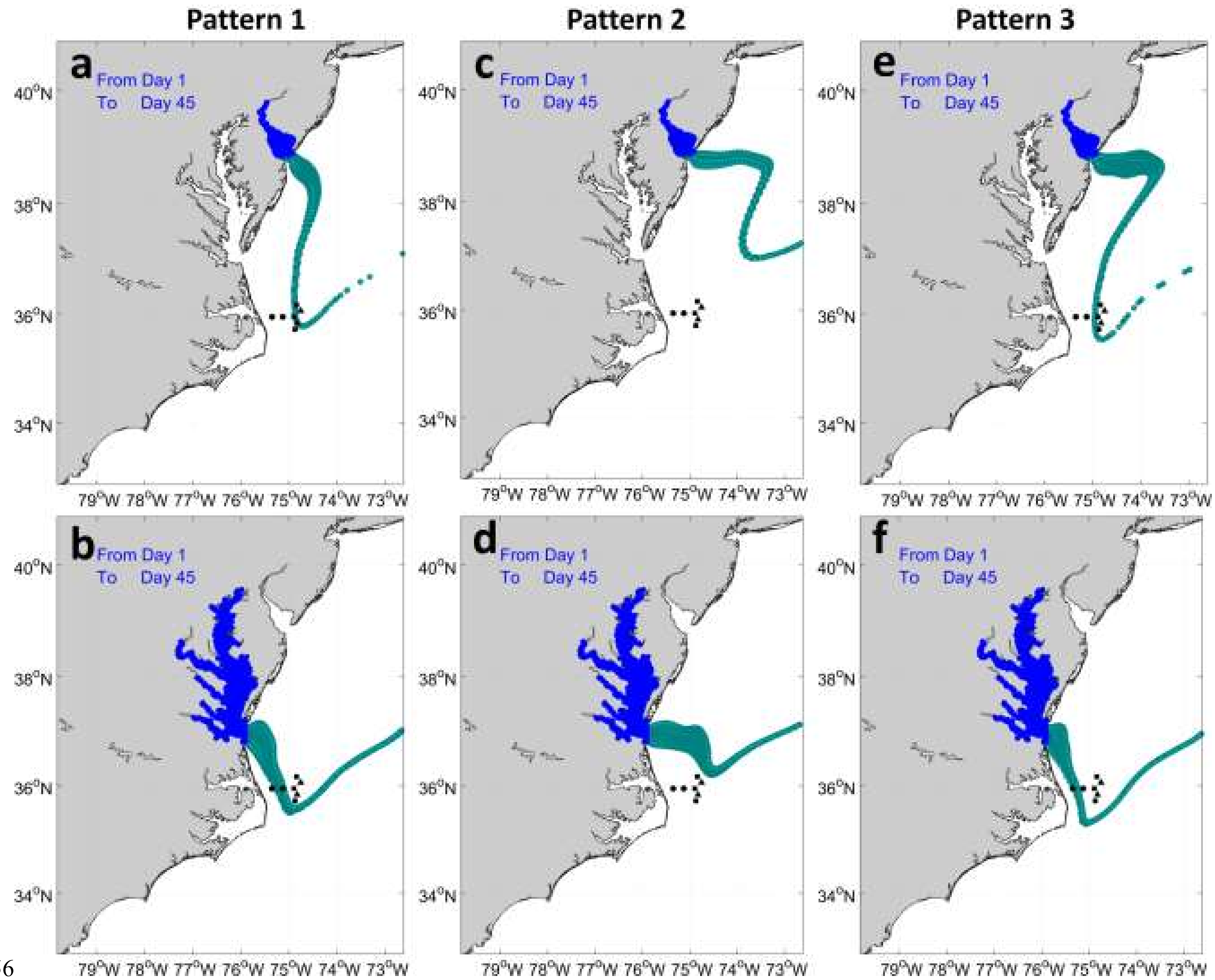

Figure 13. Movement of estuarine water particles (blue dots) from Delaware Bay (a, c, e) and Chesapeake Bay (b, d, f). The 45-day trajectories (green dots) computed from the progressive vector diagrams are driven by the composite mean sea surface velocity (SSV) fields from Figure 12, corresponding to Pattern 1 (a, b), Pattern 2 (c, d), and Pattern 3 (e, f), respectively, over 45 days. The location of the Coastal Pioneer Array in the southern MAB is shown by black dots.

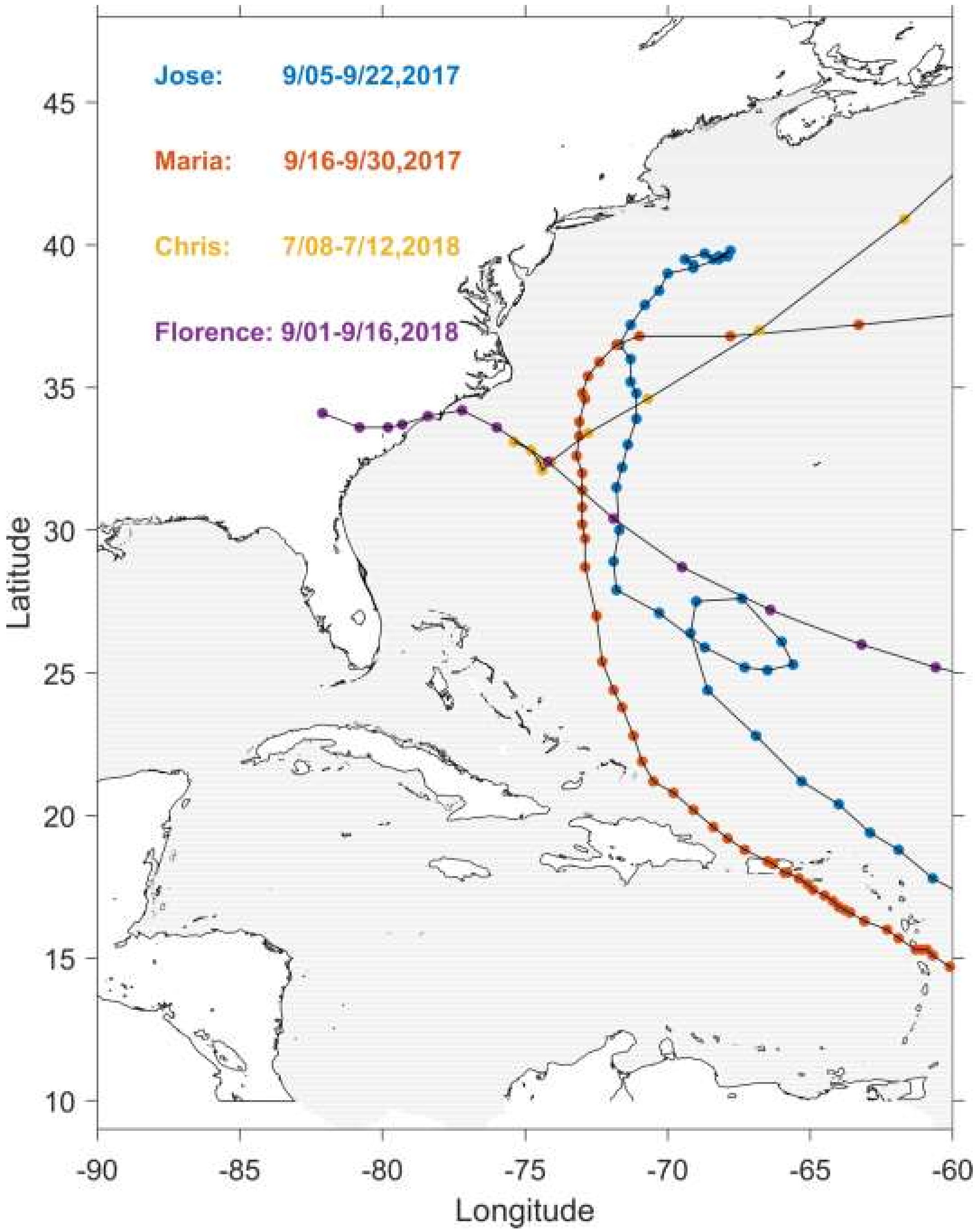

Figure 14. Hurricane paths of Jose, Maria, Chris, and Florence during the 2017 and 2018 Atlantic Hurricane seasons.

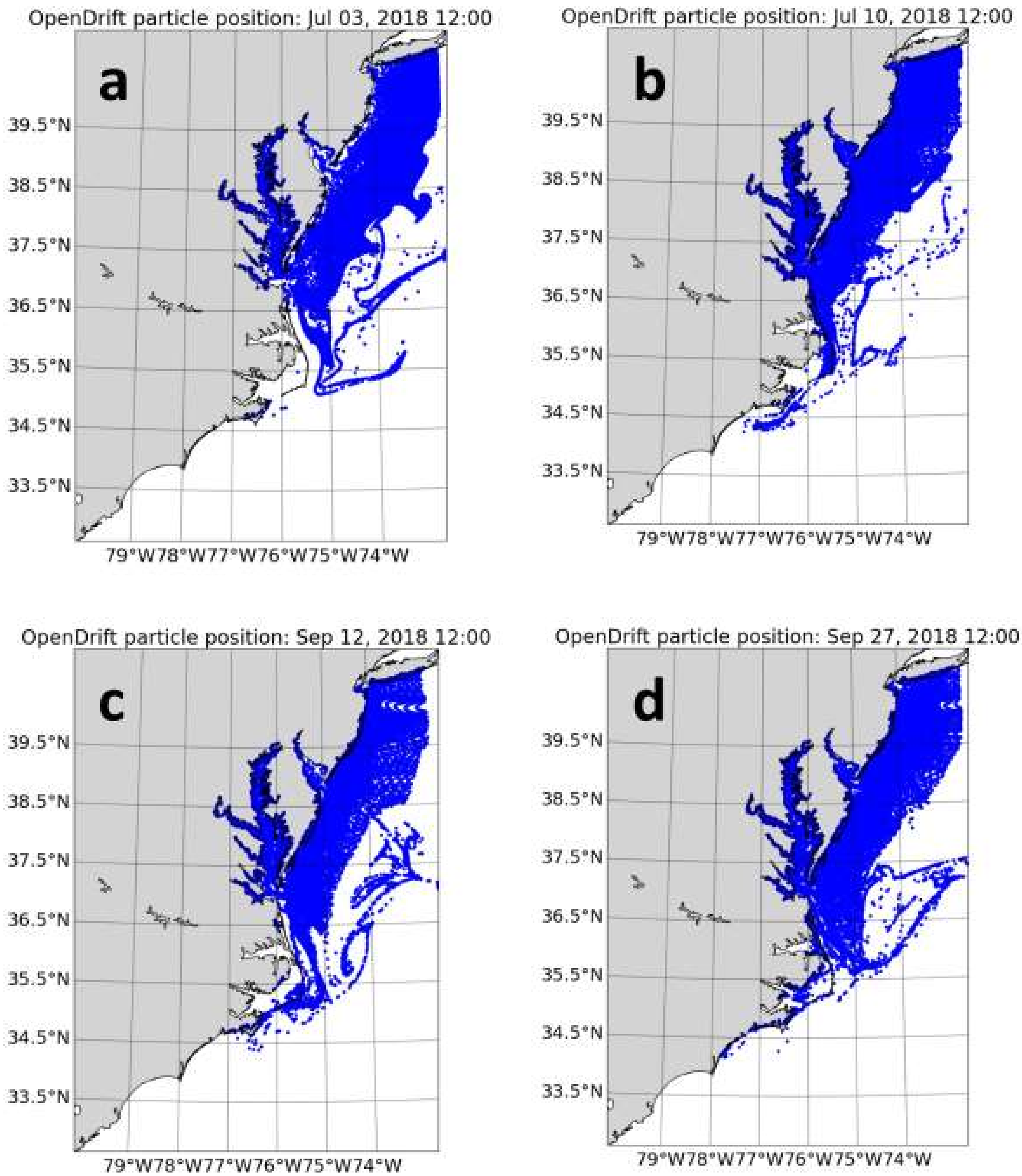

Figure 15: Panels (a), (b), (c), and (d) show the horizontal distribution of near-surface MAB shelf water on July 3, July 10, September 12, and September 27, 2018, respectively.

Table 1: Sum of Squared Errors (SSE) for Different Numbers of Clusters

Number of Clusters	Sum of Squared Errors (SSE)
1.0	268,910,336.0
2.0	223,770,432.0
3.0	199,561,136.0
4.0	189,915,488.0
5.0	184,717,632.0
6.0	180,378,976.0
7.0	175,382,544.0
8.0	173,308,048.0

References

Able, K. W. (2005). A re-examination of fish estuarine dependence: evidence for connectivity between estuarine and ocean habitats. *Estuarine, coastal and shelf science*, *64*(1), 5-17. http://doi.org/10.1016/j.ecss.2005.02.002

Andres, M. (2021). Spatial and temporal variability of the Gulf Stream near Cape Hatteras. *Journal of Geophysical Research: Oceans*, 126(9), e2021JC017579. https://doi.org/10.1029/2021JC017579

Andres, M., Muglia, M., Bahr, F., & Bane, J. (2018). Continuous flow of upper Labrador Sea water around Cape Hatteras. *Scientific Reports*, 8(1), 1-8. https://doi.org/10.1038/s41598-018-28593-x

Balthis, W. L., Hyland, J. L., Fulton, M. H., Wirth, E. F., Kiddon, J. A., & Macauley, J. (2009). Ecological condition of coastal ocean waters along the US Mid-Atlantic Bight: 2006.

Bane, J., Seim, H., Haines, S., Han, L., He, R., & Zambon, J. (2023). Atmospheric forcing of the Hatteras coastal ocean during 2017-2018: The PEACH program. *Dynamics of Atmospheres and Oceans*, 101364. https://doi.org/10.1016/j.dynatmoce.2023.101364

Brink, K. H. (2016). Cross-shelf exchange. *Annual review of marine science*, *8*, 59-78. http://doi.org/10.1146/annurev-marine-010814-015717

Berger, T. J., Hamilton, P., Wayland, R. J., Blanton, J. O., Boicourt, W. C., Churchill, J. H., & Watts, D. R. (1995). A physical oceanographic field program offshore of North Carolina, final synthesis report (*OCS Study MMS 94-0047*). New Orleans, LA: Miner. Manage. Serv., Gulf of Mex. OCS Reg., U.S. Dep. of the Inter.

Churchill, J. H., & Berger, T. J. (1998). Transport of Middle Atlantic Bight shelf water to the Gulf Stream near Cape Hatteras. *Journal of Geophysical Research: Oceans*, 103(C13), 30605-30621. https://doi.org/10.1029/98JC01842

Churchill, J. H., & Gawarkiewicz, G. G. (2012). Pathways of shelf water export from the Hatteras shelf and slope. *Journal of Geophysical Research: Oceans*, 117(C8). https://doi.org/10.1029/2011JC007228

Cowen, R. K., Hare, J. A., & Fahay, M. P. (1993). Beyond hydrography: can physical processes explain larval fish assemblages within the Middle Atlantic Bight?. Bulletin of Marine Science, 53(2), 567-587.

Dagestad, K., Röhrs, J., Breivik, Ø., & Ådlandsvik, B. (2018). OpenDrift v1.0: A generic framework for trajectory modelling. *Geoscientific Model Development*, 11(4), 1405-1420. https://doi.org/10.5194/gmd-11-1405-2018Dhanachandra, N., Manglem, K., & Chanu, Y. J. (2015). Image segmentation using K-means clustering algorithm and subtractive clustering algorithm. *Procedia Computer Science*, 54, 764-771. https://doi.org/10.1016/j.procs.2015.06.089

Dirks, R. A., Kuettner, J. P., & Moore, J. A. (1988). Genesis of Atlantic Lows Experiment (GALE): An overview. *Bulletin of the American Meteorological Society*, 69(2), 148-160. https://doi.org/10.1175/1520-0477(1988)069<0148:GOALEA>2.0.CO;2

Dugstad, J. S., Koszalka, I. M., Isachsen, P. E., Dagestad, K. F., & Fer, I. (2019). Vertical structure and seasonal variability of the inflow to the Lofoten Basin inferred from high-resolution Lagrangian simulations. Journal of Geophysical Research: Oceans, 124(12), 9384-9403 https://doi.org/10.1029/2019JC015474

Epifanio, C. E. (1995). Transport of blue crab (Callinectes sapidus) larvae in the waters off mid-Atlantic states. *Bulletin of Marine Science*, 57(3), 713-725.

Fisher Jr, A. (1972). Entrainment of shelf water by the Gulf Stream northeast of Cape Hatteras. *Journal of Geophysical Research*, 77(18), 3248-3255. https://doi.org/10.1029/JC077i018p03248

Ford, W. L., Longard, J. R., & Banks, R. E. (1952). On the nature, occurrence and origin of cold low salinity water along the edge of the Gulfstream. Journal of Marine Research,11, 281–293

Gawarkiewicz, G., Churchill, J., Bahr, F., Linder, C., & Marquette, C. (2008). Shelfbreak frontal structure and processes north of Cape Hatteras in winter. *Journal of Marine Research*, 66(6), 775-799. https://doi.org/10.1357/002224008787064754

Gawarkiewicz, G., & Linder, C. A. (2006). Lagrangian flow patterns north of Cape Hatteras using near-surface drifters. *Progress in Oceanography*, 70(2-4), 181-195. https://doi.org/10.1016/j.pocean.2006.03.019

Glenn, S. M., Miles, T. N., Seroka, G. N., Xu, Y., Forney, R. K., Yu, F., ... Kohut, J. (2016). Stratified coastal ocean interactions with tropical cyclones. *Nature Communications*, 7(1), 1-10. https://doi.org/10.1038/ncomms10887

Gulli, A., & Pal, S. (2017). Deep learning with Keras. Packt Publishing Ltd.

Haidvogel, D. B., Arango, H., Budgell, W. P., Cornuelle, B. D., Curchitser, E., Di Lorenzo, E., ... Lanerolle, L. (2008). Ocean forecasting in terrain-following coordinates: Formulation and skill assessment of the regional ocean modeling system. *Journal of Computational Physics*, 227(7), 3595-3624. https://doi.org/10.1016/j.jcp.2007.06.016

Haines, S., Seim, H., & Muglia, M. (2017). Implementing quality control of high-frequency radar estimates and application to Gulf Stream surface currents. *Journal of Atmospheric and Oceanic Technology*, 34(6), 1207-1224. https://doi.org/10.1175/JTECH-D-16-0167.1

Han, L., Seim, H., Bane, J., Savidge, D., Andres, M., Gawarkiewicz, G., & Muglia, M. (2022). Ocean circulation near Cape Hatteras: observations of mean and variability. *Journal of Geophysical Research: Oceans*, *127*(12), e2022JC019274. https://doi.org/10.1029/2022JC019274

Hare, J. A., & Cowen, R. K. (1996). Transport mechanisms of larval and pelagic juvenile bluefish (Pomatomus saltatrix) from South Atlantic Bight spawning grounds to Middle Atlantic Bight nursery habitats. Limnology and Oceanography, 41(6), 1264-1280. https://doi.org/10.4319/lo.1996.41.6.1264

He, R., and R. H. Weisberg (2003) West Florida Shelf circulation and temperature budget for the 1998 fall transition. Continental Shelf Research, 23(8), 777-800. https://doi.org/10.1016/S0278-4343(03)00028-1

Jablonski, D. (1986). Larval ecology and macroevolution in marine invertebrates. *Bulletin of marine science*, 39(2), 565-587.

Kaufman, L., & Rousseeuw, P. J. (2009). *Finding groups in data: an introduction to cluster analysis*. John Wiley & Sons.

Ketkar, N. (2017). Introduction to Keras. In F. Chollet & J. Allaire (Eds.), Deep learning with Python (pp. 97-111). Springer.

Lyard, F. H., Allain, D. J., Cancet, M., Carrère, L., & Picot, N. (2021). FES2014 global ocean tide atlas: Design and performance. *Ocean Science*, 17(3), 615-649. https://doi.org/10.5194/os-17-615-2021

Mao, S., He, R., Bane, J., Gawarkiewicz, G., & Todd, R. E. (2023a). A data-assimilative modeling investigation of Gulf Stream variability. *Deep Sea Research Part II: Topical Studies in Oceanography*, *211*, 105319. https://doi.org/10.1016/j.dsr2.2023.105319

Mao, S., He, R. and Andres, M. (2023b) Modes of North Atlantic Western boundary current variability at 36° N. *Scientific Reports* 13, 18773. https://doi.org/10.1038/s41598-023-45889-4

Mao, S, and R, He (2024a): The two-year snapshots of particle horizontal spatial distribution [Dataset], Zenodo, doi: https://zenodo.org/doi/10.5281/zenodo.10909385

Mao, S, and R, He (2024b): The two-year snapshots of particle horizontal spatial distribution image clustering codes [Software], Zenodo, doi: https://zenodo.org/records/10909386

Mao, S, and R. He (2024c): the Regional Ocean Modeling System (ROMS) configuration [Software] Zenodo . doi: https://zenodo.org/records/10961077

Mao. S and R. He (2024d): ROMS circulation output data [Dataset], DRYAD doi: https://datadryad.org/stash/dataset/doi:10.5061/dryad.280gb5mxr and doi: https://datadryad.org/stash/dataset/doi:10.5061/dryad.dv41ns260.

Moulton, M., Suanda, S. H., Garwood, J. C., Kumar, N., Fewings, M. R., & Pringle, J. M. (2023). Exchange of plankton, pollutants, and particles across the nearshore region. *Annual Review of Marine Science*, *15*, 167-202. http://doi.org/10.1146/annurev-marine-032122-115057

Nainggolan, R., Perangin-angin, R., Simarmata, E., & Tarigan, A. F. (2019, November). Improved the performance of the K-means cluster using the sum of squared error (SSE) optimized by using the Elbow method. *Journal of Physics: Conference Series*, 1361(1), 012015. https://doi.org/10.1088/1742-6596/1361/1/012015

North, E. W., Gallego, A., & Petitgas, P. (2009). Manual of recommended practices for modelling physical-biological interactions during fish early life. ICES Cooperative Research Report, (295).

Pattrick, P., & Strydom, N. (2014). Recruitment of fish larvae and juveniles into two estuarine nursery areas with evidence of ebb tide use. *Estuarine, Coastal and Shelf Science*, 149, 120-132. http://doi.org/10.1016/j.ecss.2014.08.003

Ruiz, G. M., Hines, A. H., & Posey, M. H. (1993). Shallow water as a refuge habitat for fish and crustaceans in non-vegetated estuaries: an example from Chesapeake Bay. Marine Ecology Progress Series, 1-16. https://doi.org/10.3354/meps099001

Savidge, D. K., & Austin, J. A. (2007). The Hatteras Front: August 2004 velocity and density structure. *Journal of Geophysical Research*, 112(C7). https://doi.org/10.1029/2006jc003933

Savidge, D. K., & Savidge, W. B. (2014). The Seasonal Export of South Atlantic Bight and Mid-Atlantic Bight Shelf Waters at Cape Hatteras. *Continental Shelf Research*, 74, 50–59. Elsevier BV. https://doi.org/10.1016/j.csr.2013.12.008

Savidge, D. K., Austin, J. A., & Blanton, B. O. (2013). Variation in the Hatteras Front Density and Velocity Structure Part 2: Historical Setting. *Continental Shelf Research*, 54, 106-116. Elsevier BV. https://doi.org/10.1016/j.csr.2012.11.006

Savidge, D. K., & Bane Jr, J. M. (2001). Wind and Gulf Stream influences on along-shelf transport and off-shelf export at Cape Hatteras, North Carolina. *Journal of Geophysical Research: Oceans*, 106(C6), 11505-11527. https://doi.org/10.1029/2000JC000367

Seim, H.E., D. Savidge, M. Andres, J. Bane, C. Edwards, G. Gawarkiewicz, R. He, R.E. Todd, M. Muglia, J. Zambon, L. Han, and S. Mao. (2022). Overview of the Processes driving Exchange At Cape Hatteras program. *Oceanography*. https://doi.org/10.5670/oceanog.2022.205

Shanks, A. L., & Brink, L. (2005). Upwelling, downwelling, and cross-shelf transport of bivalve larvae: test of a hypothesis. *Marine Ecology Progress Series*, *302*, 1-12. http://doi.org/10.3354/meps302001

Shchepetkin, A. F., & McWilliams, J. C. (2005). The regional oceanic modeling system (ROMS): A split-explicit, free-surface, topography-following-coordinate oceanic model. *Ocean Modelling*, 9(4), 347-404. https://doi.org/10.1016/j.ocemod.2004.08.002

Simonyan, K., & Zisserman, A. (2014). Very deep convolutional networks for large-scale image recognition. arXiv preprint arXiv:1409.1556.

Strathmann, R. R. (1985). Feeding and nonfeeding larval development and life-history evolution in marine invertebrates. *Annual review of ecology and systematics*, 16(1), 339-361. http://doi.org/10.1146/annurev.es.16.110185.002011

Todd, R. E. (2020a). Spray glider observations in support of PEACH [data set]. Scripps Institution of Oceanography, Instrument Development Group. https://doi.org/10.1575/1912/bco-dmo.813183.1

Todd, R. E. (2020b). Export of Middle Atlantic Bight shelf waters near Cape Hatteras from two years of underwater glider observations. *Journal of Geophysical Research: Oceans*, 125(4), e2019JC016006. https://doi.org/10.1029/2019JC016006

Van Sebille, E., Griffies, S. M., Abernathey, R., Adams, T. P., Berloff, P., Biastoch, A., et al. (2018). Lagrangian ocean analysis: Fundamentals and practices. Ocean Modelling, 121(November 2017), 49-75. https://doi.org/10.1016/j.ocemod.2017.11.008

Verity, P. G., Bauer, J. E., Flagg, C. N., DeMaster, D. J., & Repeta, D. J. (2002). The Ocean Margins Program: An interdisciplinary study of carbon sources, transformations, and sinks in a temperate continental margin system. *Deep Sea Research Part II: Topical Studies in Oceanography*, 49(20), 4273-4295. https://doi.org/10.1016/S0967-0645(02)00154-4

Warlen, S. M., & Burke, J. S. (1990). Immigration of larvae of fall/winter spawning marine fishes into a North Carolina estuary. Estuaries, 13, 453-461. http://doi.org/10.2307/1351789

Wellington, G. M., & Robertson, D. R. (2001). Variation in larval life-history traits among reef fishes across the Isthmus of Panama. *Marine Biology*, 138, 11-22. http://doi.org/10.1007/s002270000449

Whitfield, A. K. (2020). Littoral habitats as major nursery areas for fish species in estuaries: a reinforcement of the reduced predation paradigm. Marine Ecology Progress Series, 649, 219-234. http://doi.org/10.3354/meps13459

Zambon, J. B., He, R., Warner, J. C., & Hegermiller, C. A. (2021). Impact of SST and surface waves on Hurricane Florence (2018): A coupled modeling investigation. *Weather and Forecasting*, 36(5), 1713-1734. https://doi.org/10.1175/WAF-D-21-0003.1

Zhang, X., Munroe, D., Haidvogel, D., & Powell, E. N. (2016). Atlantic surfclam connectivity within the Middle Atlantic Bight: mechanisms underlying variation in larval transport and settlement. Estuarine, Coastal and Shelf Science, 173, 65-78. https://doi.org/10.1016/j.ecss.2016.02.019